Advanced Science

ADVANCED SCIENCE Open Access

www.advancedscience.com

RESEARCH ARTICLE OPEN ACCESS

Dense Fluorination of Nanodiamonds for Quantum Sensing

Michal Gulka[1] | Filip Steiner[1,2] | Jakub Copak[1,2] | Yuliya Mindarava[3] | Rémi Blinder[3] | Tamara Kucharikova[1] | Sang-Jun Lee[4] | Dennis Nordlund[4] | Jan Plutnar[5] | Fedor Jelezko[3,6] | Abraham Wolcott[7,8] | Stepan Stehlik[9] | Petr Cigler[1]

[1]Institute of Organic Chemistry and Biochemistry of the Czech Academy of Sciences, Prague, Czechia | [2]Department of Physical and Macromolecular Chemistry, Faculty of Science, Charles University, Prague, Czechia | [3]Institute for Quantum Optics, Ulm University, Ulm, Germany | [4]Stanford Synchrotron Radiation Lightsource, SLAC National Accelerator Laboratory, Menlo Park, California, USA | [5]Department of Inorganic Chemistry, Faculty of Chemical Technology, University of Chemistry and Technology Prague, Prague, Czechia | [6]Centre For Integrated Quantum Science and Technology (IQST), Ulm University, Ulm, Germany | [7]Department of Chemistry, San José State University, San José, California, USA | [8]Department of Physics, City College of the City University of New York, New York, USA | [9]Institute of Physics of the CAS, Prague, Czechia

Correspondence: Michal Gulka (gulka.michal@gmail.com) | Petr Cigler (petr.cigler@uochb.cas.cz)

Received: 14 July 2026 | **Revised:** 28 October 2026 | **Accepted:** 4 November 2026

Keywords: colloidal solution | fluorine | gadolinium | nanodiamond | nitrogen-vacancy center | optical sensing | spin–lattice relaxation

ABSTRACT

Shallow nitrogen-vacancy (NV) centers in high-pressure high-temperature nanodiamonds (HPHT NDs) enable nanoscale quantum sensing and bioimaging, but their charge and spin stabilities are dominated by surface chemistry. Fluorine termination of diamond is of interest because of its chemical inertness, suppression of non-specific molecular interactions, and beneficial electronic effects of NV centers. Here we establish a scalable fluorination route for HPHT NDs based on high-pressure treatment with elemental F_2. We show that pre-hydrogenation of ~28 nm HPHT NDs enables dense C—F surface termination, resulting in markedly improved NV performance. Spin-lattice relaxation times (T_1) are extended. Electron paramagnetic resonance spectroscopy reveals a ~3-fold increase in the concentration of negatively-charged NV centers, accompanied by a 2.3-fold increase in single-particle brightness. Spectral deconvolution confirms unprecedented NV^- charge stability with NV^- fraction increasing to ~94% upon fluorination compared ~57% for tri-acid oxidized NDs. Finally, taking advantage of colloidal stability of fluorinated NDs in water, we demonstrate adsorption-free, concentration-dependent detection of gadolinium (Gd^{3+}) in chelated electroneutral form (gadoteridol) using in-solution T_1 relaxometry. These results establish fluorination as an effective strategy to stabilize shallow NV centers and expand the utility of NDs for quantitative sensing in aqueous environments.

1 | Introduction

Nanodiamonds (NDs) doped with nitrogen-vacancy (NV) centers have attracted considerable attention as promising tools for applications in bioimaging and quantum biosensing. Their biocompatibility, photostability, and ability to host optically addressable spin defects make them great candidates for biomarkers and nanoscale sensors of temperature and magnetic and electric fields [1–5]. For such applications, it is particularly desirable to use shallow NV centers, located close to the surface of NDs, because they ensure strong interaction with the surrounding environment. However, the optical and spin properties of shallow NV centers are strongly affected by the surface termination of NDs, which determines the charge stability of NV centers and, consequently, fluorescence contrast and sensing performance [6–9].

Michal Gulka and Filip Steiner contributed equally.

This is an open access article under the terms of the Creative Commons Attribution License, which permits use, distribution and reproduction in any medium, provided the original work is properly cited.
© 2026 The Author(s). *Advanced Science* published by Wiley-VCH GmbH

More generally, NV performance in NDs is governed by bulk defects, particle morphology, and the near-surface electronic structure, making surface engineering central to optimizing these quantum nanomaterials [10]. For shallow NV centers, dangling bonds and other paramagnetic surface species enhance spin relaxation, while charge traps, residual sp^2 carbon, adsorbates, strain, and structural disorder generate magnetic and electric-field noise, destabilize the NV charge state, and shorten spin relaxation and coherence times [10, 11]. Surface termination further controls the surface dipole, electron affinity, and band bending, thereby shifting NV charge-transition levels relative to the Fermi level; electron-accepting surface states can deplete shallow NV centers, whereas suitable termination and passivation can stabilize NV^- [10]. Consequently, a chemically well-defined and homogeneous surface is essential for reproducible control of the electronic and spin environment of near-surface NV centers [10, 12].

The chemical groups present on the surfaces of ND particles thus play a decisive role in determining the electronic environment around NV centers [13, 14]. Surface termination can therefore be viewed as a means of simultaneously engineering surface chemistry and the near-surface electronic structure. Among the possible atomic terminations of diamond (e.g., with hydrogen [15, 16], oxygen [17] or nitrogen [18, 19]), fluorination is among the few that have been repeatedly associated with a significant positive effect on the optical stability of NV centers [20–24]. Moreover, even mild fluorination appears to synergistically enhance already well-oxidized ND surfaces: Previous work on the selective substitution of surface carboxyl groups produced mixed oxygen/fluorine hydrophilic terminations [24], and despite the low overall fluorine content, these surfaces still showed improved stabilization of the negatively charged NV^- state.

The unique way fluorination affects carbon-based materials arises from the extreme electronegativity of fluorine, which reshapes surface dipoles, influences band bending and consequently modifies optical and electronic properties, and additionally from its chemical stability enhancing chemical resistance of the materials [25–28]. With regard to diamond, fluorination is particularly intriguing for three main reasons: First, it contributes to surface stabilization, as C—F bonds possess very high bond energies, comparable to those found in aliphatic fluorocarbons, and are chemically inert. Second, fluorination reduces molecular interactions of external chemical species in solution: A continuous C—F layer, as demonstrated for fluorinated diamond-like carbon, suppresses interactions with both polar molecules (such as water and proteins) [29] and hydrophobic species. This peculiar surface "polar hydrophobicity" [30] manifests also as the fluorous effect, which is the ability to interact preferentially with densely fluorinated molecules and structures [31]. Third, fluorination affects band bending at the diamond surface, which is critical for modulating the charge state and optical behavior of near-surface NV centers [14, 20–24]. In this respect, dense fluorination represents a particularly well-defined limit of surface electronic-structure engineering, in which a strongly electronegative termination can simultaneously passivate surface carbon sites and modify the electrostatic boundary conditions experienced by shallow NV centers. Additionally, the fully fluorinated diamond surface has been proposed as a main building block for large-scale quantum simulators owing to its uniformity and compatibility with the reliable initialization, control, and readout of NV centers [32].

In bulk or thin-film diamonds, partial fluorination has been achieved using different strategies, including treatment with elemental fluorine (F_2), ClF_3 [33] or XeF_2 [34], X-ray irradiation of perfluoroalkyl iodide layers on the surface followed by thermal decomposition [35], or plasma-assisted methods (using CF_4 or SF_6) [23, 36, 37]. Among these, SF_6 plasma has proven particularly effective for chemical vapor deposition (CVD) diamond, yielding high-quality, homogeneous fluorine coverage. Plasma fluorination can provide rapid surface conversion; for example, efficient replacement of oxygen by fluorine during short CF_4-plasma treatment was observed [38]. However, prolonged CF_4-plasma exposure also resulted in surface roughening, facet-dependent etching, increasing crystal-defect density, and evidence of minor fluorocarbon-polymer formation [38]. Similarly, $Ar/O_2/SF_6$ plasma processing is intrinsically coupled to diamond etching, and the resulting surface roughness and nanostructure formation depend strongly on treatment time, SF_6 content, and plasma conditions [39]. In contrast, direct F_2 fluorination does not involve energetic plasma bombardment or fluorocarbon plasma precursors and therefore avoids these plasma-specific pathways of surface damage and deposition.

However, preparative plasma-based fluorination of ND particles, which are typically agglomerated, is inherently limited by the accessibility of plasma-generated reactive species. Whereas thermal fluorination with F_2 gas proceeds via diffusion of reactive species into nanoparticle agglomerates, plasma-generated species approach externally exposed surfaces only, which leads to heterogeneous, surface-biased functionalization. Moreover, nanoparticles in plasma accumulate electrostatic charge, leading to repulsion or levitation and loss of material to chamber walls, which results in poor process control and reduced yield. These considerations make direct gas-phase fluorination particularly attractive for preparative fluorination of ND powders, despite the demanding handling requirements associated with elemental F_2.

Fluorination has been reported for various types of NDs, which exhibit distinct chemical reactivities. Detonation nanodiamonds (DNDs) possess a highly defective diamond structure with sp^2-coordinated carbon species distributed throughout the particle volume, including twin boundaries, stacking faults, and defect-rich regions [40, 41], which confers a higher and chemically different type of reactivity than high-pressure high-temperature (HPHT) or CVD diamond. Whereas the fluorination of DNDs has been investigated using a variety of approaches [42–47], these cannot be readily translated to the predominantly single-crystalline and generally larger HPHT and CVD diamond. HPHT microdiamond and ND particles have been fluorinated using 10% F_2 in He at 340°C [48] and HPHT microdiamond further using CF_4 plasma [49], elemental F_2 [33, 50, 51] at various temperatures, or by reaction with F_2 or ClF_3 [33]. Alternative strategies involve reactions with fluorinating agents such as Selectfluor [24], chlorination of the diamond surface followed by a reaction with CHF_3 at 600°C [52], and electron beam irradiation in the presence of NF_3 [22].

Motivated by the broad interest in HPHT NDs as sites of NV centers for quantum sensing and bioimaging, we investigate surface fluorination with the aim of enhancing their optical properties. To maximize the efficiency of fluorination, we use highly reactive F_2 under elevated pressure and temperature and

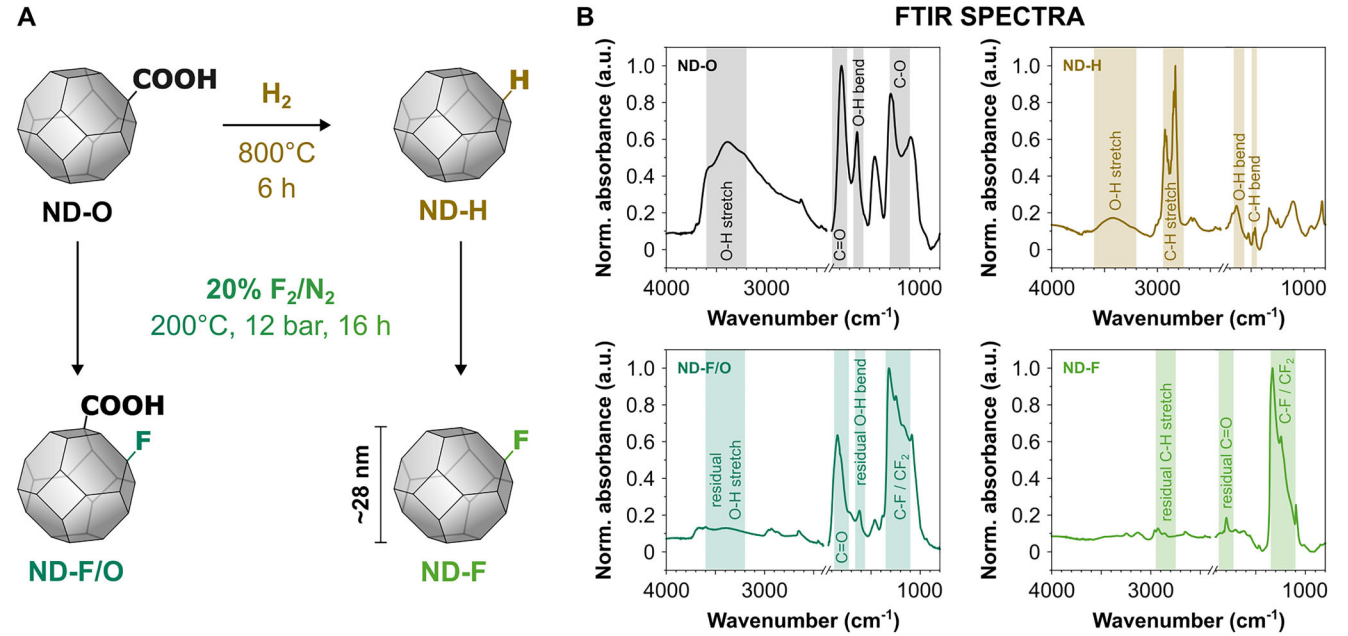

FIGURE 1 | (A) Scheme depicting the two fluorination routes used here, employing oxidized (**ND-O**) and hydrogenated (**ND-H**) nanodiamond particles as precursors for elemental F_2 fluorination yielding a mixed F/O (**ND-F/O**) and fluorinated (**ND-F**) surface, respectively. (B) FTIR spectra of the four samples prepared in this study (**ND-O**, **ND-H**, **ND-F/O** and **ND-F**) with their characteristic features highlighted.

systematically investigate how the initial surface chemistry of NDs, namely their starting termination with oxygen and hydrogen, influences their reactivity toward fluorination (Figure 1A). The surfaces of fluorinated particles are characterized using Fourier-transform infrared (FTIR) spectroscopy, X-ray photoelectron spectroscopy (XPS), and X-ray absorption spectroscopy (XAS). Furthermore, we study the effect of fluorination on NV properties using confocal fluorescence microscopy and electron paramagnetic resonance (EPR) spectroscopy. Our results provide detailed insight into how fluorination can be used as part of a preparative method to stabilize NV centers and optimize their performance for sensing and bioimaging applications.

2 | Results and Discussion

2.1 | Starting Surfaces for ND Fluorination

We used oxygen- and hydrogen-terminated ND surfaces as precursors for fluorination. To create oxidized NDs, we chose the common and well-defined approach of air oxidation, removing sp^2 carbon, followed by tri-acid oxidation, introducing COOH groups to the ND surface [53]. Such NDs are colloidally stable and exhibit good NV properties [54]. The Fourier transform infrared spectroscopy (FTIR) spectrum of the oxidized ND sample (**ND-O**) shows characteristic bands of oxygen-containing surface groups (Figure 1B). A broad O–H stretching mode, due to adsorbed water and covalent O—H, is observed in the range 3200–3600 cm^{-1}, accompanied by an O—H bending vibration near 1630 cm^{-1}. The strong carbonyl (C═O) stretching evident at ~1780 cm^{-1}, and C—O and C—OH related modes between 1100–1300 cm^{-1} confirm the presence of oxygen-containing surface groups on **ND-O**, consistent with a mixed oxidized surface resulting from the combined air and tri-acid oxidation treatment [54, 55].

For hydrogenation, we chose a thermal route [56, 57], rather than hydrogen plasma treatment. Compared to plasma-based approaches, thermal hydrogenation provides a more uniform treatment of powder samples, avoids cross-contamination in plasma chambers, and requires only equipment commonly available in standard chemical laboratories. To create hydrogenated NDs (**ND-H**), the **ND-O** was treated in a hydrogen atmosphere of H_2 gas for 6 h at 800°C at atmospheric pressure [58], converting most surface functionalities into C—H bonds. Hydrogenation manifests itself in the appearance of dominant C–H features (C–H stretching vibrations at 2850–2950 cm^{-1}, C—H bending modes at ~1450–1500 cm^{-1}) and a significant reduction of oxygen-containing bands in the FTIR spectrum (Figure 1B). A weak O–H stretching contribution persists in the 3200–3600 cm^{-1} region, consistent with a residual content of OH groups and/or adsorbed water. Corresponding changes are also evident in X-ray photoelectron spectroscopy (XPS) (Figure 2A), where the O 1s intensity decreases strongly for **ND-H** compared to **ND-O**, which is consistent with the replacement of oxygen functionalities by hydrogen.

We further characterized the samples by X-ray absorption spectroscopy (XAS) in total electron yield (TEY) mode, a synchrotron-based technique that is element-specific and surface-sensitive, probing up to approximately 10 nm deep into a material. The electronic structure of HPHT ND is similar to that of the bulk crystal, showing a sharp signal from the diamond core-hole exciton at 289 eV and a second band gap at 302 eV (Figure 2B,C) [60]. Signals from $\pi^*_{(C=C)}$ and $\pi^*_{(C=O)}$ transitions (285.0 and 286.8 eV) in the C 1s spectra of all samples are negligible and confirm the dominant sp^3-C character of the samples. The O 1s spectrum (Figure 2D) of **ND-O** shows characteristic $\pi^*_{(C=O)}$ and $\sigma^*_{(C-O)}$ signals (~531.5 and ~537 eV) originating from various oxygen-containing groups formed after the three-acid oxidative treatment, consistent with the FTIR analysis. These oxygen

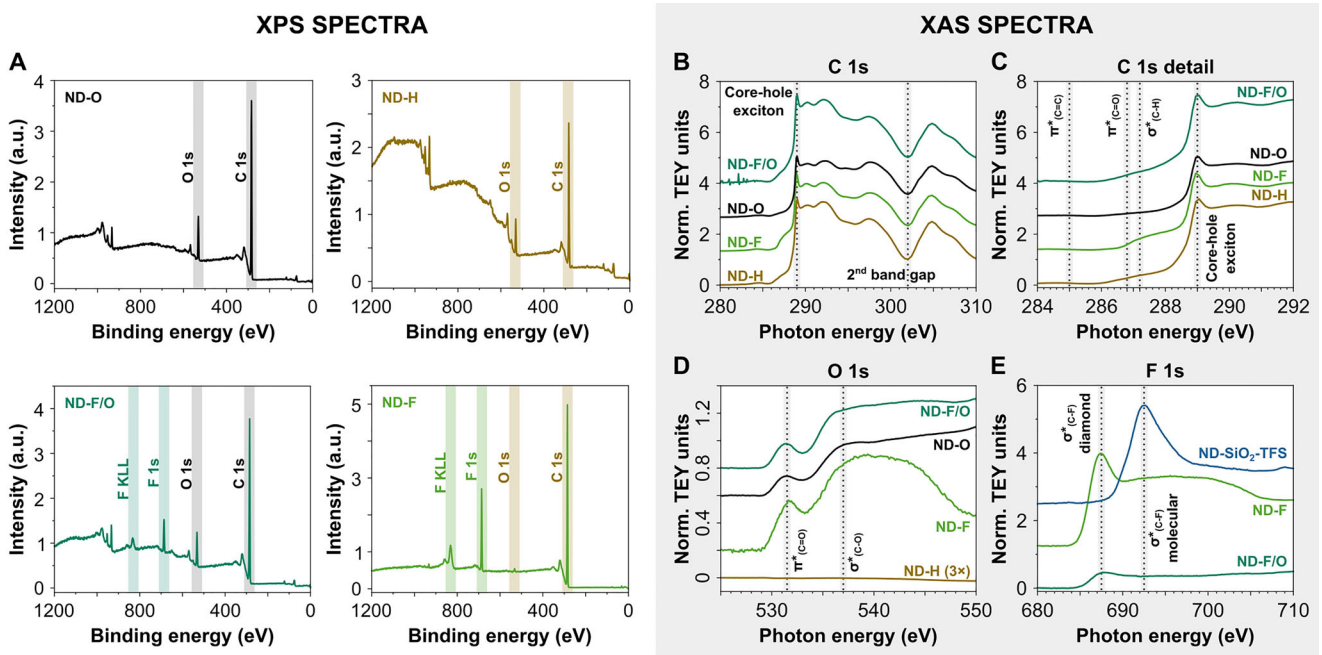

FIGURE 2 | XPS and XAS spectra of the starting materials (**ND-O** and **ND-H**) and the corresponding fluorinated products (**ND-F/O** and **ND-F**). (A) Wide-range XPS spectra of all samples. See Table 1 for calculated fluorine and oxygen content and the Supporting Information for a deconvolution of C 1s spectra. (B) C 1s XAS spectrum and (C) detail of its core-hole exciton region. Shoulders at 285.0, 286.8, and 287.2 eV are assigned to the $\pi^*_{(C=C)}$, $\pi^*_{(C=O)}$, and $\sigma^*_{(C-H)}$ resonances, respectively. (D) O 1s and (E) F 1s XAS spectra measured in total electron yield (TEY) mode. The F 1s XAS spectrum of silica-coated NDs functionalized with 3,3,3-trifluoropropyltrimethoxysilane (i.e., the **ND-SiO$_2$-TFS** sample) is reproduced with permission from the raw data of ref [59] (Copyright 2023, American Chemical Society) and is presented for comparison only. The lower energy of the diamond–fluorine bond hints at increased stability and could be a consequence of the extended structure present in diamond in contrast to a single-molecule analogue. The XAS spectra are offset for clarity. The **ND-H** spectrum in D) is multiplied by a factor of 3.

resonances are absent in the **ND-H** sample (note that the signal is multiplied by a factor of three) and confirm a homogeneously hydrogenated ND surface.

2.2 | Fluorinated NDs

Considering the inherently low reactivity of the HPHT ND surface and the need to achieve high surface coverage, we used gaseous F_2 treatment under relatively harsh conditions (200°C, 12 bar, 16 h, 20 % F_2 in N_2). Both **ND-O** and **ND-H** samples reacted with F_2 to form covalent C–F bonds and were labeled **ND-F/O** and **ND-F**, respectively. Fluorination of the oxidized ND surface (**ND-F/O**) significantly suppresses the O–H stretching and bending bands while, at the same time, introducing new peaks associated with fluorinated species (Figure 1B). The spectrum exhibits well-defined C–F stretching modes in the 1100–1300 cm^{-1} region, as well as distinct features attributed to CF_2 and possibly CF_3 groups in the ~1200–1350 cm^{-1} range. However, carbonyl vibrations shifted to 1840 cm^{-1} remain, demonstrating only partial conversion of oxygen-containing groups. By contrast, fluorination of the hydrogenated ND surface (**ND-F**) leads to complete removal of the O–H stretching signal and nearly complete disappearance of the O–H bending band. Strong and sharp C–F stretching vibrations dominate in the 1100–1300 cm^{-1} region, together with pronounced CF_2 and possibly CF_3 group absorptions between ~1200 and ~1350 cm^{-1}. Only weak residual signals from carbonyl and alcohol groups are detectable, indicating that fluorination of **ND-H** is much more effective than fluorination of **ND-O**. These results are consistent with previously observed reactivity of hydrogenated and oxidized HPHT microdiamonds towards F_2 [50]. Once the ND surface is fluorinated, it has excellent chemical stability—FTIR spectra remeasured after almost two years remain practically unchanged (Figure S3).

The XPS spectra provide further confirmation of the surface chemistry modifications upon fluorination, with new peaks characteristic of fluorinated species becoming evident (Figure 2A). Specifically, the **ND-F/O** spectrum displays distinct F 1s and F KLL lines alongside the residual O 1s signal, confirming that fluorination of the oxidized surface proceeds only partially. By contrast, the **ND-F** spectrum demonstrates an almost complete disappearance of the O 1s signal and the emergence of strong F 1s and F KLL peaks. These observations are consistent with the FTIR results, confirming that fluorination after oxidation results in partial surface conversion, whereas fluorination following hydrogenation leads to the near-complete replacement of surface groups by fluorine species. Detailed XPS spectra and their analysis are provided in the Supplementary Information (Figure S2).

The fluorination manifested clearly in the XAS spectra and can be compared to that of fluorinated small molecules. First, the K-edge fluorine spectra (Figure 2E) clearly show the $\sigma^*_{(C-F)}$ transition in both fluorinated samples (687.5 eV), which points to tertiary alkyl fluoride, referred to as lattice-bound F. For comparison, we

TABLE 1 | Summary of physicochemical, optical and EPR characteristics of NDs with different surface terminations. EA stands for elemental analysis.

Sample	Description	EA F (%)	XPS F (%)	XPS O (%)	XPS F/(F+O) (%)	Optical Properties NV^- fract. (%)	Optical Properties ND PL (kcts./s)	Optical Properties T_1 (µs)	EPR NV conc. (ppm)	EPR P1 conc. (ppm)
ND-O	Tri-acid oxidized	0.16	0.00	8.02	0	57	160 ± 20	220 ± 40	1.2 ± 0.2	1.2 ± 0.2
ND-H	Hydrogenated	0.17	0.00	8.08	0	N.A.	N.A.	N.A.	N.A.	N.A.
ND-F/O	Fluorinated ND-O	2.96	4.67	6.42	42	87	250 ± 40	280 ± 60	3.6 ± 0.5	3.0 ± 0.6
ND-F	Fluorinated ND-H	5.82	10.47	0.92	92	94	360 ± 50	310 ± 60	3.5 ± 0.5	2.3 ± 0.5

show the F 1s spectrum of an ND sample bearing a nanolayer of fluorinated siloxane (**ND-SiO_2-TFS**) taken from another study [59], where the $\sigma^*_{(C-F)}$ transition appears at 692.5 eV, which is consistent with primary alkyl fluoride (—CF_3). The 5 eV difference in the $\sigma^*_{(C-F)}$ transition is significant and indicates a degree of stabilization of the diamond–fluorine bond. The lower energy edge in both **ND-F** and **ND-F/O** samples suggests that lattice-bound F forms more covalent C—F bonds (i.e., bonds with lower polarization), in line with the high thermal stability of F-terminated diamond surfaces [35]. The higher degree of fluorination in the **ND-F** sample compared to **ND-F/O** is further reflected in the higher intensity of $\sigma^*_{(C-F)}$ signals in both the C 1s and F 1s spectra. Despite the low intensity of the O 1s signal in the XPS spectrum of **ND-F**, the XAS O 1s spectrum of **ND-F** contains a clear $\sigma^*_{(C-O)}$ and $\pi^*_{(C=O)}$ transition. This is consistent with residual —COOH and C—OH groups identified based on FTIR measurements. We hypothesize that the remaining diamond–oxygen groups that have withstood the fluorination at 200°C are very stable, even though they likely can be converted at even higher reaction temperatures [50].

Elemental analysis (see the Methods section, Table 1 and Table S1) corroborates the spectroscopic evidence for extensive fluorine incorporation. Within experimental uncertainty, the measured fluorine content for the starting **ND-O** and **ND-H** materials is at background level, whereas both fluorinated samples contained substantial amounts of fluorine (2.96% and 5.82% for **ND-F/O** and **ND-F**, respectively). The transmission electron microscopy (TEM)m images suggest that the harsh conditions during the fluorination do not induce any measurable etching. The TEM-calculated size distributions (Figure 3A) show that all samples exhibit similar average particle sizes of 26–29 nm (equivalent circular diameters). Raman spectra measured with 355 nm excitation confirmed a dominant sp^3 diamond band at 1332 cm^{-1} for all samples (Figure 3B), indicating that no graphitization occurred during fluorination. A weak G band corresponding to sp^2 carbon is present only in the **ND-H** spectrum, consistent with the surface rearrangement due to the thermal hydrogenation [61]. Overall, the surface chemistry of the starting material is crucial for the conversion and the resulting surface composition. The advantage of hydrogenation lies in the high chemical homogeneity of the **ND-H** surface and its enhanced reactivity, enabling near-quantitative conversion to C—F groups.

To estimate the surface coverage of lattice-bound fluorine, we employed geometric models of the NDs based on TEM analysis. While the TEM-derived equivalent diameters of particles can be estimated with good precision from the projected TEM areas, a principal uncertainty in such calculations arises from reconstructing the three-dimensional particle shape from two-dimensional TEM projections. A further uncertainty concerns the crystallographic identity of the exposed facets, as substantial {111} facet exposure has been reported for ball-milled HPHT NDs [55], whereas the main facet of similarly sized (∼25 nm) NDs has been preferentially assigned to {110} [62]. We therefore considered the surface-site densities of both facets and compared a simple spherical approximation with a disk-like model reflecting the pronounced anisotropy of these particles [62–64] (see the Supporting Information for derivation). The commonly used spherical approximation produced high, nonphysical fluorine coverages of 149%–182% for **ND-F** and 70%–86% for **ND-F/O**, depending on the assumed surface facets (Table S2). By contrast, the disk-like model, based on the aspect ratio of 5.2 estimated from experimental data [62, 63], yielded physically plausible but slightly underestimated fluorine coverages (62%–76% for **ND-F** and 29%–36% for **ND-F/O**), as the real particles shape is more elliptic rather than cylinder [65]. The vast differences between the two models underscore how strongly the absolute coverage estimates depend on the assumed particle geometry. For strongly anisotropic nanoparticles such calculations should be thus regarded as mere approximate.

In this specific case, XPS, which determines the relative atomic concentrations within the near-surface region, provides complementary estimate of the relative degree of fluorine surface termination, as it is less dependent on particle-shape assumptions. While XPS cannot directly quantify hydrogen termination and therefore cannot provide a complete comparison of surface-site occupancies in hydrogenated and oxidized samples, it is particularly informative for the present fluorinated surfaces. For instance, **ND-F** contains 10.5 at.% F and only 0.92 at.% O. The ratio F/(F+O) provides an apparent fluorine fraction of 92% for **ND-F** and 42% for **ND-F/O** (Table 1), assuming that F and O account for most non-hydrogen surface terminations and approximately represent equivalent surface-site populations. These values are qualitatively consistent with the trends observed by FTIR, XAS, and elemental analysis. This estimate remains subject to systematic uncertainties arising

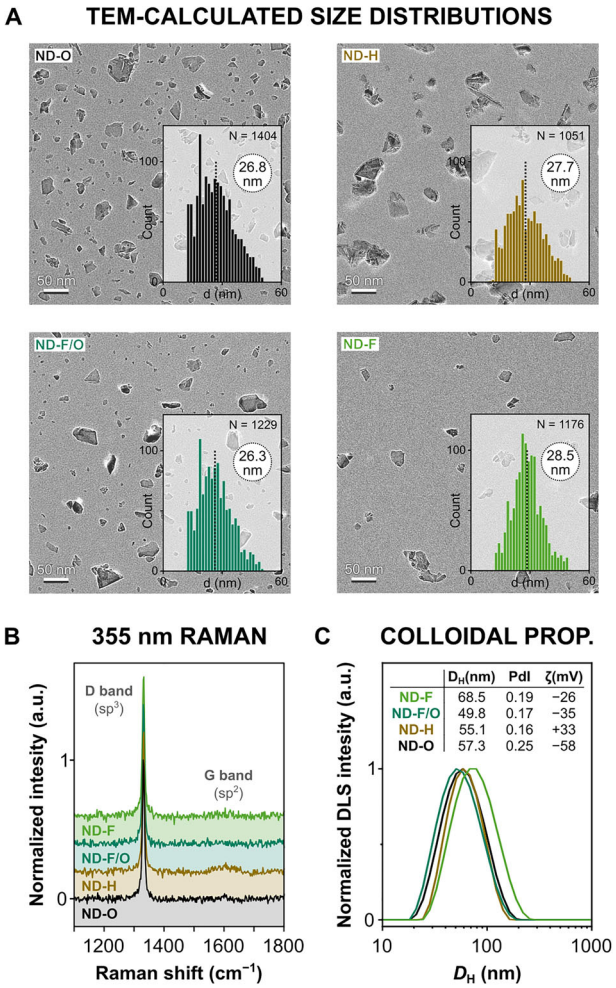

FIGURE 3 | Material and colloidal properties of the NDs under study. (A) TEM images and corresponding size distributions of the various NDs studied. Although the ND-H sample tended to aggregate on the TEM grid, its aggregates were excluded from the size analysis to avoid biasing the particle size distribution. (B) Normalized Raman spectra (355 nm excitation) show a characteristic diamond band at 1332 cm^{-1} (sp^3 carbon) and a weak G band (sp^2 carbon) for the **ND-H** sample. (C) Normalized volume-weighted dynamic light scattering (DLS) distributions. The overall narrow size distributions indicate that all samples, including ones after fluorination, are colloidally stable in water. However, thorough probe-sonication was required to disperse fluorinated samples (see the Methods section). The table presents the resulting hydrodynamic diameter (D_H), polydispersity index (PdI) and measured zeta potential (ζ).

from XPS acquisition and quantification, including background subtraction, peak fitting, sensitivity factors, and sampling effects. Adsorbed water would increase the detected O signal and therefore lead to underestimation of the apparent fluorine fraction. Conversely, any residual hydrogen termination, which is not captured by XPS, would lead to an overestimation of the fluorine fraction. However, the very weak C–H-related FTIR signal of the fluorinated samples suggests that this contribution is limited. Nevertheless, all independent estimates consistently indicate approximately twofold higher fluorination of **ND-F** than of **ND-F/O**.

2.3 | Colloidal Properties of Fluorinated NDs

The starting **ND-O** sample shows a characteristic size distribution in aqueous solution as measured by dynamic light scattering (DLS) and highly negative (−58 mV) zeta potential (Figure 3C). Hydrogenation led to a positive zeta potential of **ND-H** (+33 mV) as expected [58]. After fluorination, both samples exhibited a negative zeta potential similar to that observed for fluorinated graphene oxide [66]. The **ND-F/O** sample (−35 mV) still contained a significant amount of carbonyl groups, and the negative zeta potential was sufficient to keep the particles in a non-aggregated state. Notably, the extensively fluorinated **ND-F** particles (−26 mV) remained dispersible in water after thorough probe-sonication (Methods), forming stable colloids over a prolonged timescale (remeasured after about six months). In principle, complete fluorination may suppress interactions with both polar and hydrophobic molecules [29]. We attribute the dispersibility in water to a combination of residual polar surface sites (e.g., edge/vertex oxidation during aqueous work-up) and electrostatic stabilization, as indicated by the negative zeta potential. Although a modest increase in the apparent hydrodynamic size suggests some degree of association, no macroscopic precipitation was observed. Additionally, we examined the colloidal stability of fluorinated NDs in different fluorous phases–fluorinated solvents of different polarity and chain length. The results are discussed in the Supporting Information. We also anticipate that the fluorous effect of the surface C—F moieties [31] could also provide an advantageous platform for the recently demonstrated NV-center-based NMR detection of polyfluoroalkyl substances in water sources [67].

2.4 | Effect of Fluorination on NV Center Properties

A fully-fluorinated diamond surface provides the highest positive electron affinity [34] and is therefore expected to significantly stabilize the NV^- charge state due to band bending near the ND surface. As a result, even smaller (sub-50 nm) ND particles are expected to have stable NV-related luminescence and the total number of bright NVs per particle is expected to increase. Additionally, charge stabilization might help to reduce charge cycling in the dark, caused, for example, by NV ionization and recombination processes [68], which are detrimental to optical T_1 relaxometry readout [69].

To test these hypotheses, we first carried out continuous-wave (CW) electron paramagnetic resonance (EPR) spectroscopy, which is a reliable method for quantifying negatively charged NV centers in NDs. NV^- concentrations were estimated from the intensity of the half-field EPR signal ($g \sim 4$), which is considerably narrower than the anisotropic $g \sim 2$ spectrum and therefore allows for more accurate spin quantification [70, 71] (see Supporting Information). Both fluorinated samples showed a pronounced increase in NV signal intensity, yielding approximately threefold greater values of NV concentration compared to the starting **ND-O** material (Figure 4A). Similarly, the concentration of substitutional nitrogen in its neutral charge state N_S^0 (P1 centers) increased after fluorination likely by conversion from N_S^+ (see Table 1 and the Supplementary Information). Overall,

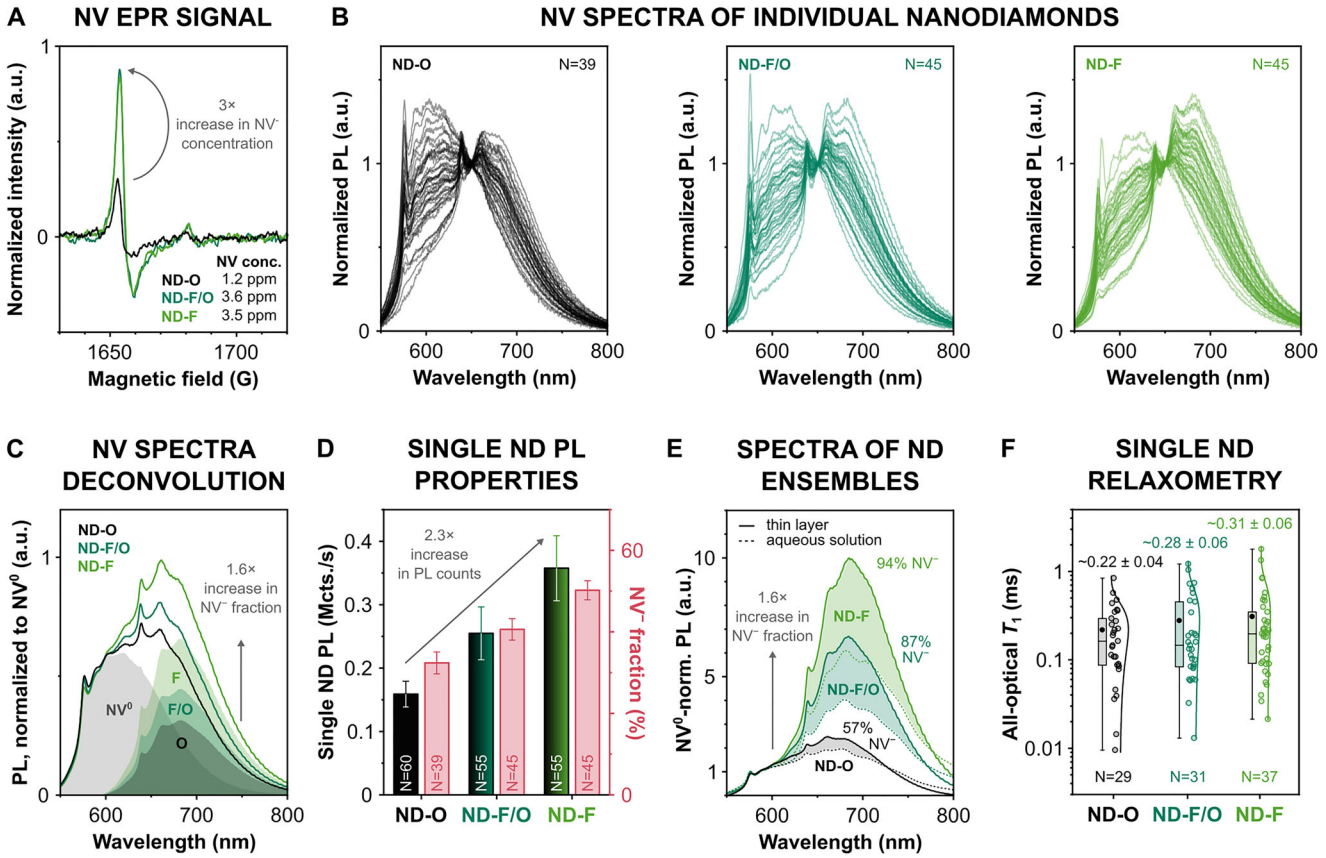

FIGURE 4 | Effect of fluorination on the properties of NV-containing NDs. (A) Mass-normalized first-derivative X-band CW EPR spectra in the half-field transition region of NV^- centers, showing a pronounced increase in NV^- signal intensity in fluorinated ND samples. (B) Normalized single-particle PL spectra with different surface terminations, showing increased NV^- emission after fluorination. (C) NNMF deconvolution of particle-weighted average PL spectra reveals a ~1.6-fold increase in the NV^- fraction upon fluorination. (D) Average single-particle PL count rates (left axis) and single-particle NV^- fractions from NNMF (right axis) for NDs with different surface terminations. Fluorination increases both the PL intensity and the NV^- fraction by up to 2.3-fold. Standard errors are reported. (E) PL spectra of ND ensembles normalized to the NV^0 emission peak with varying surface terminations, demonstrating an increased NV^- fraction upon fluorination (from 57% to 94%) in the thin layer. (F) All-optical spin-lattice relaxation times (T_1) of single NDs with different surface treatments. Fluorinated NDs exhibit longer T_1 times, indicating improved spin properties. Means and standard errors are reported.

these observations suggest a general stabilization of electron-rich defect charge states near the ND surface upon fluorination due to downward band bending.

We further studied the NV photoluminescence (**PL**) properties of the materials at the single-particle level. Colloidally stable solutions were spin-coated on glass coverslips and the spectra of individual particles were measured in a confocal configuration (Figure 4B). The spectra were then normalized using a trapezoidal rule integral and averaged for each sample, yielding particle-weighted spectral averages. All normalized and averaged spectra were analyzed jointly. Non-negative matrix factorization (NNMF) as implemented in Matlab was used to deconvolute the spectra and calculate the NV^- and NV^0 contributions to the PL signal [64]. However, it has recently been suggested [72] that simple NNMF underestimates the contribution of NV^0 because it does not fit the NV^0 PL tail at longer wavelengths, meaning that the deconvoluted NV^0 signal ends at around 700 nm [73]. Here, instead, we developed a semi-supervised NNMF using typical measured reference NV^- and NV^0 spectra as initial values for the deconvolution, resulting in significantly improved fits to the dataset. We note that, as a consequence of better NV^0 fit, the resulting NV^- fractions are lower compared to the standard NNMF we used previously [19, 73] (Figure 4C). A clear trend in the stabilization of the NV^- charge state is observed with increasing levels of surface fluorination, reaching an approximately 1.6-fold increase in the NV^- fraction of **ND-F** compared to **ND-O**. This increase in the NV^- charge state of individual particles (Figure 4D, right y-axis) is accompanied by an increase in PL counts (Figure 4D, left y-axis). To measure the brightness of individual NDs, the filtered PL (long-pass 650 nm) from diffraction-limited spots was detected on a single-photon counting detector and integrated. The photon counts per particle increased by approximately 2.3-fold between oxidized **ND-O** and fluorinated **ND-F**.

In addition to single-particle measurements, we compared the PL spectral properties of ND ensembles (Figure 4E). The spectra were recorded both from thin layers (solid lines) and from aqueous solutions (dotted lines) and normalized to the NV^0 emission peak. The same clear trend is consistently observed across configurations, as fluorination significantly stabilizes the NV^-

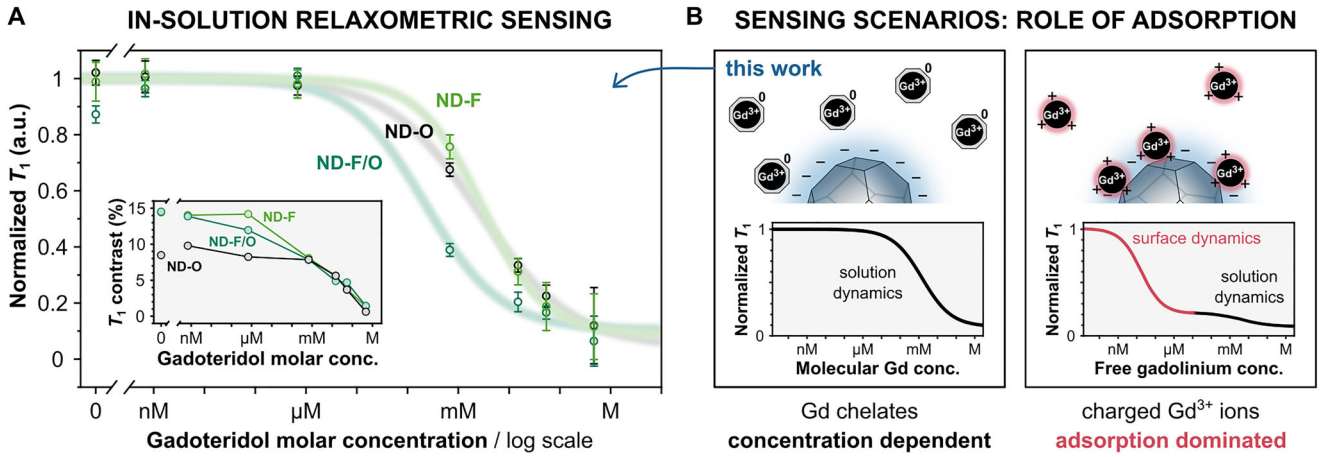

FIGURE 5 | In-solution relaxometry using gadoteridol at various concentrations as the spin target. A) Dependence of the T_1 relaxation times of **ND-O**, **ND-F/O** and **ND-F** on the concentration of gadoteridol. The inset shows the T_1 contrast, which decreases with increasing gadoteridol concentration, as expected [77]. Representative T_1 data are shown in Figure S6. (B) Schematic illustration of the different sensing regimes. The left panel shows the solution-dynamics-dependent T_1 response when using non-ionic chelates as employed in the present study. The right panel depicts the surface-dynamics-dominated detection observed in previous works using free Gd^{3+} [76].

charge state in all of them. When included in the NNMF analysis, the resulting NV^- fractions obtained by thin-layer measurements were 57% for **ND-O** and 87% for **ND-F/O**. Particularly noteworthy is the enhancement for the fluorinated **ND-F** sample, reaching 94% NV^- emission, which corresponds to an approximately 1.6-fold improvement compared to **ND-O**. Such strong NV^- stability in small NDs is, to our knowledge, unprecedented and highlights the importance of the surface optimization treatment of NDs.

The results of all-optical spin-lattice relaxation measurements suggest systematic T_1 improvement with increasing fluorine content (Figure 4F). The mean T_1 values increase from ~0.22 ms for **ND-O** to ~0.28 ms for **ND-F/O** and ~0.31 ms for **ND-F**. Although the improvement seems significant, we note that NV charge decay within the dark time of the T_1 sequence can effectively mask proper readout [68, 69, 74]. Even though great care was taken to omit such compromised measurements (using a previously developed methodology [54]), these results should still be interpreted with caution and serve primarily as an indication that fluorination does not impair NV spin relaxation. To further test the application potential of fluorinated NDs as quantum probes, we performed a concentration-dependent, in-solution sensing experiment with gadolinium(III).

2.5 | Gadoteridol Sensing Using In-Solution Relaxometry

We prepared ND solutions with various concentrations of Gd^{3+} as a paramagnetic source and performed in-solution T_1 relaxometry (Figure 5A). However, as has been well documented in recent studies [75, 76], free Gd^{3+} ions get strongly adsorbed to the negatively charged ND surface. As a consequence, the measured response is dominated by an adsorption mechanism (surface-site saturation), producing non-linear concentration dependences consistent with Langmuir-type adsorption models. This leads to the detection being primarily sensitive to adsorbed rather than freely dissolved Gd^{3+}, saturating already at sub-micromolar Gd^{3+} concentrations (Figure 5B, right panel). To decouple in-solution concentration-dependent dynamics from adsorption-driven surface effects, we used electroneutral gadolinium chelate gadoteridol, which prevents adsorption to ND surface.

Gadoteridol is a non-ionic, macrocyclic gadolinium(III) chelate that serves as a clinically approved MRI contrast agent. Its macrocyclic coordination confers high complex stability and helps keep gadolinium in a well-defined chelated form in aqueous solution. Being hydrophilic and electroneutral, it strongly suppresses charge-driven adsorption onto NDs, and the T_1 measurements therefore reflect solution dynamics saturating at submolar rather than submicromolar concentrations (Figure 5B, left panel). The resulting concentration-dependent T_1 detection depicted in Figure 5A provides, to our knowledge, the first ND-based in-solution relaxometry measurement of gadolinium performed in this adsorption-minimized chelated regime. The results suggest slightly better sensitivity of the mixed **ND-F/O** surface, whereas **ND-O** and **ND-F** yielded similar results. The advantage of fluorinated ND surfaces lies in higher PL counts and greater T_1 contrast, both shortening the measurement time. Fluorination may also reduce general non-specific adsorption onto the ND surface owing to the weakly interacting nature of the fluorine termination.

3 | Conclusions

We have developed a robust fluorination protocol for HPHT NDs, based on high-pressure F_2 treatment, and demonstrated that the initial surface chemistry critically determines the extent of the conversion. Pre-hydrogenation enables near-quantitative replacement of surface groups by lattice-bound C—F species, most likely by enhanced and uniform reactivity of C—H bonds with F_2. Extensive fluorination substantially improves NV-center

performance by increasing the NV^- concentration (~3×) and sample brightness (~2.3×) and by stabilizing the NV^- charge state (94% NV^- fraction) to levels not common for small ~28-nm NDs. Finally, using the electroneutral chelate gadoteridol, we have demonstrated the applicability of concentration-dependent in-solution T_1 relaxometry in an adsorption-minimized regime, highlighting the potential of fluorinated NDs for quantitative sensing in complex aqueous environments. For applications requiring biomolecular targeting, future work will focus on controlled heterofunctionalization through the selective replacement of small fractions of surface fluorine with reactive anchoring groups while preserving the fluorine-rich surface that stabilizes NV centers. Given the fundamental chemical similarity of HPHT and CVD diamond surfaces, we anticipate that this high-pressure gas-phase fluorination strategy can be readily extended to other single-crystalline diamond nanostructures and thin-film architectures.

4 | Methods

4.1 | Chemicals and Solvents

NDs were purchased from Pureon AG (Microdiamant MSY 0–0.05). Sulfuric acid (H_2SO_4), nitric acid (HNO_3), perchloric acid ($HClO_4$), sodium hydroxide (NaOH), and hydrochloric acid (HCl) were obtained from Lach-Ner (Czechia). Hexafluoroisopropanol, perfluorohexane, perfluorooctane, and gadoteridol were purchased from Merck Life Science (Merck, Czechia). Milli-Q water was used in all solutions and washing steps.

4.2 | Preparation of ND-O Sample

2.0 g of NDs were first homogenized using an agate mortar and then thermally air-oxidized in a tube furnace at 540°C for 6 h under ambient air, with manual mixing every 20 min. After cooling to room temperature, approximately 1.8 g of gray air-oxidized powder was obtained. Next, 1 g of the NDs was ground in an agate mortar with a pestle and transferred into a polytetrafluoroethylene (PTFE) vessel. Subsequently, 6 mL of each concentrated acid (H_2SO_4, $HClO_4$, and HNO_3) was added for acid oxidation. The suspension was sonicated for 10 min in a bath sonicator, and then heated to 90°C for 48 h under continuous stirring. The mixture was cooled after the reaction, divided into two Falcon tubes placed on ice and centrifuged at 3969 g for 15 min (25°C). The supernatants were discarded and the pellets were resuspended in water. NDs were washed with water, 1M NaOH, water, 1M HCl, and again with water under the same conditions. ND colloidal solution was then split into six centrifuge tubes and subjected to six consecutive washing cycles with water at 30 000 g for 25 min (25°C). The resulting colloid was lyophilized to yield approximately 0.8 g of ND powder. This material was evenly spread on a thick aluminum target and irradiated using an electron beam for 80 h (16.5 MeV, 4 C/cm^2, maximum sample temperature 60°C). After irradiation, the powder was annealed at 900°C for 1 h under an argon atmosphere. The sample was then subjected again to the same oxidative treatment (air oxidation at 540°C for 6 h followed by three-acid oxidation at 90°C for 48 h) and finally lyophilized, affording approximately 600 mg of ND-O powder.

4.3 | Preparation of ND-H Sample

NDs were hydrogenated in a tube furnace at 800°C under a continuous flow of hydrogen at atmospheric pressure. Samples (~800 mg) were heated at a ramp rate of 8°C min^{-1} and maintained at the target temperature for 6 h with a hydrogen flow rate of 25 mL · min^{-1}. The treatment resulted in a mass loss of ~8 wt.%, consistent with the replacement of oxygen-rich surface functionalities by lighter C—H_x groups.

4.4 | Preparation of ND-F/O and ND-F Samples

Both ND-F/O and ND-F samples were prepared using the same fluorination procedure; ND-O was used as the starting material for ND-F/O, while ND-H served as the precursor for ND-F. Fluorination was carried out on a dedicated fluorination line described in the Supporting Information (Figure S1). ND powder (500 mg) was placed into a PTFE reaction chamber, which was inserted into a Monel autoclave (400 mL internal volume). The autoclave was closed, evacuated, and flushed with nitrogen. This evacuation/N_2-flush cycle was repeated five times to ensure the removal of oxygen and moisture. After the final evacuation, the autoclave was slowly filled with a 20 % F_2/N_2 gas mixture and pressurized to 12 bar at room temperature. F_2 gas is toxic, readily reacts with water in the atmosphere, and extreme caution should be used when handling. The autoclave was then heated to 200°C and kept at this temperature overnight. After cooling to room temperature, the gaseous reaction products were released into waste-collection cylinders and neutralized. The autoclave was again flushed with nitrogen and evacuated (five cycles). After the final N_2 filling, the autoclave was opened, and the fluorinated NDs were collected from the PTFE reactor. The ND powder was transferred into a 100 mL round-bottom flask, heated to 120°C and kept under vacuum overnight to desorb any residual HF, yielding approximately 465 mg of ND-F/O or ND-F powder.

4.5 | FTIR Spectroscopy

Fourier-transform infrared (FTIR) spectra were acquired using a Bruker Vertex V70 spectrometer equipped with a diamond ATR accessory. Approximately 1–3 mg of ND powder was placed directly onto the ATR crystal, and spectra were recorded against the background spectrum of the clean diamond prism. Measurements were performed in the 800–4000 cm^{-1} range using a room-temperature DLaTGS detector. Each spectrum represents 128 scans collected at a spectral resolution of 4 cm^{-1} under ambient laboratory conditions. Due to the strong intrinsic multi-phonon absorption of the diamond ATR crystal in the 1900–2400 cm^{-1} region, this part of the spectra is affected by an instrument-specific background pattern and is omitted from the graphical presentation (Figure 1B).

4.6 | X-ray Photoelectron Spectroscopy (XPS)

XPS measurements were performed using a SPECS instrument equipped with a monochromatic Al K_α X-ray source (1486.7 eV) and a Phoibos 150 hemispherical analyzer. The samples were

suspended in dry acetonitrile and drop-cast onto a copper tape anchored to the sample holder. The process was repeated several times until a homogeneous spot of the sample with a diameter of approximately 5 mm was formed. Survey spectra were collected at a pass energy of 100 eV, and high-resolution core-level spectra were recorded at 30 eV. The chamber pressure during acquisition was $\leq -10^{-9}$ mbar. Surface charging was compensated for using a low-energy electron flood gun (30 μA, 3.5 eV).

4.7 | X-ray Absorption Spectroscopy (XAS)

XAS measurements were performed at beamline 8–2 of the Stanford Synchrotron Radiation Lightsource at the SLAC National Accelerator Laboratory, using a spot size of $< 1\,mm^2$. All samples were handled in open-air conditions and mounted to an Al sample bar with conductive carbon tape (#16073-4 Ted Pella, Inc. Redding, CA). Samples were introduced into the analysis chamber after the transfer chamber reached 1×10^{-7} Torr. The conditions inside the analysis chamber were typically set at 5×10^{-9} Torr. Colloidal samples were deposited on piranha-etched gold coated silicon wafers with a 5 nm Ti adhesion layer (LGA thin films Santa Clara, CA). The wafer size was 10×10 mm and 200 μL of a 1 mg/mL solution was deposited onto a piranha-etched wafer. The samples were heated to 50°C with a hotplate to accelerate the rate of evaporation while being covered with a crystallization dish to prevent contamination from the atmosphere. ND samples were mounted onto an Al sample bar using conductive carbon tape without further preparation. At beamline 8–2, C, N, and O K-edge XAS was measured in total electron yield mode using 42×42, 40×40, and 30×30 μm slits, respectively. This mode probes up to approximately 10 nm of the sample depth, and all experiments were conducted under ultrahigh vacuum conditions ($\sim 5 \times 10^{-9}$ Torr). After focusing the optics, the reference absorption intensity of the incoming X-ray beam was measured using a sample of gold-coated mesh and used to correct for beam instability. XAS data were collected at an incident electric field vector of 54.7°. For spectral analysis, the data were treated with linear pre-edge background subtraction from a region before the absorption edge of C, N, and O at 260–280, 370–380, and 510–530 eV, respectively. Post-edge normalization was also performed in the continuum region at 340 eV for C, 420 eV for N, and 580 eV for O, using a batch processing macro in Igor Pro. Energy calibration was performed using the signal from the diamond core-hole exciton, which was determined to be 289.0 eV as described elsewhere.

4.8 | Elemental Analysis (EA)

EA of carbon, hydrogen, and nitrogen was performed using a PE 2400 Series II CHNS/O Analyzer (PerkinElmer, USA). Samples were combusted at 925°C, converting the elements into simple gases (CO_2, H_2O, and N_2). The samples were weighed into tin capsules using an analytical microbalance (Cubis MSA 6.6S, Sartorius, Germany). The generated gases were homogenized and brought to defined pressure, temperature, and volume conditions before being released through a separation column, where they were resolved in a stepwise steady-state mode and detected based on their thermal conductivities. Each sample was measured in triplicate, and the results are reported as means ± their standard deviation ($n = 3$).

4.9 | Determination of Fluorine Content

The content of F was quantified using a selective fluoride ion electrode (ORION 25–092) and a potentiometric ion-selective electrode (ISE) method. Samples were combusted using the Schöniger procedure, and the combustion products were absorbed in distilled water. A total ionic strength adjustment buffer (TISAB) was added to ensure constant ionic strength and appropriate measurement conditions. The electrode potential (mV) was recorded using the fluoride ISE and a reference electrode, and fluoride concentrations were determined from a calibration curve prepared from standard fluoride solutions. The determination was performed without replicates.

4.10 | Transmission Electron Microscopy (TEM) and Image Analysis

Bright-field TEM imaging was carried out using a JEOL JEM-2100Plus microscope operated at 200 kV. Samples were prepared on commercial copper grids (SPI, 300 mesh regular grid) coated with parlodion and an additional carbon layer. The grids were first placed on a 20 μL droplet of poly(ethyleneimine) solution (M_W 2.5 kDa, 0.1 mg/mL) for 10 min (10 s for the ND-F sample), gently blotted, and transferred onto a 20 μL water droplet for 1 min. After blotting, the grids were placed on a 20 μL droplet of ND aqueous dispersion (0.1 mg/mL) for 10 min, blotted again, and dried for 30 min in a Petri dish. TEM image analysis was performed using an in-house MATLAB script to extract particle size distributions. Background noise was reduced using an isotropic Gaussian smoothing filter (*imgaussfilt*, $\sigma = 1.6$), followed by automated contrast adjustment (Image Segmenter app). Initial particle masks were generated using the Auto Cluster segmentation method and refined by morphological dilation and closing operations. Objects touching the image borders were removed (*imclearborder*), and incorrectly identified features were manually excluded. Segmented particles were labeled with pseudorandom colors for visualization (*label2rgb*). Each labeled object represented either a single primary particle or a multi-particle aggregate. To prevent multi-particle aggregates from skewing the primary particle size distribution, all interconnected clusters and overlapping aggregates were algorithmically excluded during image segmentation, followed by manual inspection and exclusion of remaining potential aggregate structures from quantification. For size analysis, 1000–1500 particles (after exclusion of invalid objects) were evaluated. Projected areas were extracted using the *regionprops* function. Equivalent circular diameters (d) were calculated from the projected area (S) according to $d = 2\sqrt{(S/\pi)}$.

4.11 | Sample Sonication for Colloidal Stability of the NDs

Approximately 1 mg of ND powders were weighed into separate 2 mL Eppendorf tubes and Milli-Q water was added to obtain a final concentration of 0.5 mg/mL. Suspensions were probe-sonicated using a 750 W, 20 kHz ultrasonic homogenizer (Cole-Palmer, 230 V model). The sonication time was 1–2 h, using

a 1 s on/1 s off pulse mode at 20% amplitude. To prevent overheating, an ice-ethanol bath was used throughout the sonication. After sonication, the samples were centrifuged at 2500 g for 2 min to remove impurities originating from the probe tip.

4.12 | Dynamic Light Scattering (DLS) and Zeta Potential (ZP)

DLS and ZP measurements were performed at room temperature using a Zetasizer Nano ZS (Malvern Instruments). Concentrations of ND samples were 0.1 mg/mL. Each sample was measured in triplicate using disposable folded capillary cells (DTS1070), and results are reported as means ± standard deviation (n = 3). Zeta potential was determined in 0.1 mM NaCl to ensure constant conductivity. For measurements in fluorinated solvents, the corresponding viscosity and refractive index values at 25°C were applied: hexafluoroisopropanol (1.65 cP, 1.275), perfluorohexane (0.64 cP, 1.252), and perfluorooctane (1.80 cP, 1.284). These measurements were performed as single determinations.

4.13 | Electron Paramagnetic Resonance

Electron paramagnetic resonance (EPR) measurements were performed using a Bruker Elexsys E580 spectrometer operating in the X-band frequency range (9–10 GHz). Continuous-wave (CW) EPR with an ER-4122-SHQE resonator was employed to estimate P1 and NV spin concentrations. NV coherence times were measured using pulsed EPR with a FlexLine ER-4118X-MD5 resonators

4.14 | PL and Raman Measurements of Thin ND Layers

The PL (Figure 4E) and Raman (Figure 3B) spectral measurements were carried out using a commercial WITec alpha300R confocal Raman microscope. A thin layer of NDs was deposited by drop-casting an ND aqueous solution (1 µL droplet of 0.2 mg/mL) on a silicon substrate followed by evaporation at 55°C; this procedure was repeated 60 times. The NV luminescence spectra were acquired for 20 s at 8 random spots using a 10× ZEISS EC Epiplan objective (N.A. = 0.25) and a 532 nm laser with a power of 200 µW (measured before the objective) and averaged. Spectra were detected using an Andor CCD camera coupled with a WITec UHTS300 spectrometer (150 lines/mm, grating blazed for 500 nm). Raman spectra were acquired for 50 s at 8 random spots using a Thorlabs LMU-40X-NUV MicroSpot objective (N.A. = 0.47) and a 355 nm laser with a power of 1 mW (measured before the objective) and averaged. Raman signals were detected using an Andor CCD camera coupled with a WITec UHTS400 spectrometer (1200 lines/mm, grating blazed for 300 nm).

4.15 | Single-Particle Spectral and T_1 Measurements

The PL and T_1 characterization of the individual NDs (Figure 4B–D,F) were performed using a commercial WITec alpha300R confocal Raman microscope modified to enable pulse laser excitation and time-resolved single-photon detection. Cover glasses were sonicated in beakers with tetrahydrofuran, ethanol, methanol, and MilliQ water (in that order) using a sonication bath and dried. Subsequently, they were cleaned for 30 min in a UV Ozone Cleaner (BioForce ProCleaner). To deposit NDs on the cover glass a 10 µL of 10 µg/mL aqueous ND solution was spin-coated dynamically at 1000 rpm using a vacuum-free Ossila Spin Coater. The PL from individual ND particles was excited by a 532 nm laser of 44 µW power (measured before the objective) focused through an oil objective (Olympus UPLAPO100XOHR, N.A. = 1.5). Spectra were measured from diffraction-limited spots and detected using an Andor CCD camera with a WITec UHTS300 spectrometer (150 lines/mm, grating blazed for 500 nm). The total integration time depended on the signal intensity and was set to reach a sufficient signal-to-noise ratio. Before each measurement, a custom-written LabView routine was performed to automatically optimize the XYZ position of the piezo stage so that the beam was in the middle of the particle. After the measurements, a semi-supervised non-negative matrix factorization was carried out in MATLAB for NV spectral deconvolution and is further described in the main text. For the measurements of PL intensity and T_1 relaxometry the PL was filtered using a 650 nm long-pass filter and detected by a single-photon counting avalanche photodiode. To obtain PL intensity (counts/s) of individual NDs the signal was averaged for a duration of ∼1 min. Before the measurements, the XYZ position of the piezo stage was optimized. Additionally, for the T_1 acquisition, subsequent optimization steps were performed every 4 min during the measurements. The pulse sequence used for T_1 acquisition consisted of laser pulses (12 µs), which were used for NV spin initialization to $m_s = 0$, as well as for spin readout by integrating the signal (spin contrast) at the beginning of the laser pulse (200–400 ns readout window) and normalizing it to the polarized NV signal at the end of the same laser pulse (∼2000 ns readout window). The resulting decay curves were fitted with single-exponential decay functions to obtain T_1 spin relaxation constants. The PL intensity and T_1 relaxometry measurements were controlled using custom-written LabView software.

4.16 | Spectral Measurements of ND Aqueous Solutions in Cuvettes

ND aqueous solutions were diluted in Milli-Q water to reach a final concentration of 0.1 mg/mL. PL spectra were measured from a quartz cuvette filled with 200 µL of ND solution under excitation from a green solid-state laser (Cobolt Fandango, 515 nm, 100 mW) excitation using a home-made micro-spectroscopy setup with an imaging spectrometer (Hamamatsu C10027-02). The spectra were recorded for 1 s with 120 accumulations and averaged. A control sample of the filtered MilliQ water was measured under the same conditions, and the resulting spectra were subtracted from the ND spectra presented in Figure 4E.

4.17 | In-Solution T_1 Relaxometry for Gadoteridol Sensing

For the preparation of samples containing gadoteridol, 12.00 µL of 0, 940, 108, 30, 1.36, 1.36, 1.36 nM gadoteridol solutions, 3.75 µL of Milli-Q water, and 2.25 µL of the ND colloidal solution (0.5 mg/mL) were mixed in a 1.5 mL Eppendorf tube

to create solutions with final gadoteridol concentrations of 0, 627, 72, 20, 0.9, 0.9, 0.9 nM, respectively. The concentrations of the 940, 108, 30 mM gadoteridol solutions were confirmed by inductively coupled plasma mass spectrometry (ICP-MS). The resulting mixture was sonicated for 2 min using a cup-horn sonicator (750 W, 20 kHz ultrasonic homogenizer, Cole-Palmer, 230 V model) operated in a 2 s on/2 s off pulse mode at 100% amplitude. A 0.8 mm thick adhesive silicone isolator with a round well opening was attached to the cleaned cover glass. The well was filled with 7 µL of ND aqueous solution and sealed with another cover glass, forming a "micro-cuvette". The in-solution T_1 characterization of the colloidal NDs was carried out using commercial WITec alpha300R confocal Raman microscope modified to enable pulse laser excitation and time-resolved single photon detection. The sample was excited by focusing a 532 nm laser of 10 mW power (measured before the objective) through an air objective (Zeiss EC Epiplan-Neofluar 2.5×, N.A. = 0.06). The PL signal was filtered through a 731/137 nm bandpass filter and detected with a single-photon counting avalanche photodiode. The Z-focus was optimized to maximize the PL signal. The T_1 pulse sequence consisted of laser pulses (50 µs) for initialization of the NV centers into the $m_s = 0$ state and, subsequently, for the readout of the resulting NV spin state. The spin population was measured by integrating the PL signal (spin contrast) at the beginning of the laser pulse (1500–3000 ns readout window) and normalizing it to the polarized NV signal at the end of the same laser pulse (5000 ns readout window). The T_1 data were fitted with stretched exponential decay functions to obtain spin relaxation times. The measurements were controlled using custom-written LabView software.

Author Contributions

Michal Gulka: investigation, writing – original draft, funding acquisition, methodology, visualization, writing – review and editing, formal analysis, supervision. **Filip Steiner**: investigation. **Jakub Copak**: investigation. **Yuliya Mindarava**: investigation, writing – original draft. **Rémi Blinder**: investigation. **Tamara Kucharikova**: investigation. **Sang-Jun Lee**: investigation. **Dennis Nordlund**: investigation. **Jan Plutnar**: investigation. **Fedor Jelezko**: supervision, funding acquisition. **Abraham Wolcott**: investigation, writing – original draft. **Stepan Stehlik**: investigation, writing – review and editing, funding acquisition. **Petr Cigler**: conceptualization, funding acquisition, methodology, writing – review and editing, writing – original draft, supervision.

Acknowledgements

Jitka Libertinova and Elisabeth Zaluska are acknowledged for the processing of samples and FTIR spectra measurements, respectively. The project was supported by Czech Science Foundation Project No. 26–21785S, by the Czech Academy of Sciences – Strategy AV21 grant program VP29, European Union project C-QuENS (Grant Number. 1101135359), Horizon Europe MSCA-SE project FLORIN (grant agreement ID 101086142), the Technology Agency of the Czech Republic project TH90010001 EXTRASENS (ERA-NET/QuantERA Cofund Project), and by the Operational Programme Johannes Amos Comenius under the Ministry of Education, Youth and Sports of the Czech Republic (MEYS CR) project CZ.02.01.01/00/22_008/0004558 Advanced Multiscale Materials for Key Enabling Technologies. We acknowledge the CzechNanoLab Research Infrastructure supported by the MEYS CR (LM2023051). A.W. would like to acknowledge support from the CREST-IDEALS Center (NSF-2112550). The use of the Stanford Synchrotron Radiation Lightsource, SLAC National Accelerator Laboratory was supported by the U.S. Department of Energy, Office of Science, Office of Basic Energy Sciences under contract DE-AC02-76SF00515. Fedor Jelezko is supported by the German Federal Ministry of Research, Technology and Space (BMFTR) via future cluster QSENS DIAQNOS (No. 13N16463), quNV2.0 (No. 13N16707), Deutsche Forschungsgemeinschaft (DFG) via projects 387073854, 445243414, 491245864, 546850640, 560722984, and joint DFG/JST ASPIRE program via project 554644981, European Union's HORIZON Europe program via projects CQuENS (No. 101135359), QCIRCLE(No. 101059999) and FLORIN (No. 101086142), QuantERA ERA-NET Cofund in Quantum Technologies via AQuSeND project, European Research Council (ERC) via Synergy grant HyperQ (No. 856432), and Carl-Zeiss-Stiftung via Research Center QPhoton and project Ultrasens-vir.

Conflicts of Interest

The authors declare no conflicts of interest.

Data Availability Statement

The data that support the findings of this study are openly available in Zenodo at https://doi.org/10.5281/zenodo.22904296, reference number 22904296.

References

1. J. Su, Z. Kong, L. Zeng, et al., "Fluorescent Nanodiamonds for Quantum Sensing in Biology," *WIREs Nanomedicine and Nanobiotechnology* 17, no. 3 (2025): 70012, https://doi.org/10.1002/wnan.70012.

2. Y. Wu, F. Jelezko, M. B. Plenio, and T. Weil, "Diamond Quantum Devices in Biology," *Angewandte Chemie International Edition* 55, no. 23 (2016): 6586–6598, https://doi.org/10.1002/anie.201506556.

3. T. Zhang, G. Pramanik, K. Zhang, et al., "Toward Quantitative Bio-Sensing with Nitrogen–Vacancy Center in Diamond," *ACS Sensors* 6 (2021): 2077.

4. G.-Q. Liu, R.-B. Liu, and Q. Li, "Nanothermometry with Enhanced Sensitivity and Enlarged Working Range Using Diamond Sensors," *Accounts of Chemical Research* 56, no. 2 (2023): 95–105, https://doi.org/10.1021/acs.accounts.2c00576.

5. J. Barton, M. Gulka, J. Tarabek, et al., "Nanoscale Dynamic Readout of a Chemical Redox Process Using Radicals Coupled With Nitrogen-Vacancy Centers in Nanodiamonds," *ACS Nano* 14, no. 10 (2020): 12938–12950, https://doi.org/10.1021/acsnano.0c04010.

6. M. B. A. Olia, P. S. Donnelly, L. C. L. Hollenberg, P. Mulvaney, and D. A. Simpson, "Advances in the Surface Functionalization of Nanodiamonds For Biological Applications: A Review," *ACS Applied Nano Materials* 4 (2021): 9985.

7. T. Rosskopf, A. Dussaux, K. Ohashi, et al., "Investigation of Surface Magnetic Noise by Shallow Spins in Diamond," *Physical Review Letter* 112, no. 14 (2014): 147602, https://doi.org/10.1103/PhysRevLett.112.147602.

8. W. Zhang, J. Zhang, J. Wang, et al., "Depth-Dependent Decoherence Caused by Surface and External Spins for NV Centers in Diamond," *Physical Review B* 96, no. 23 (2017): 235443, https://doi.org/10.1103/PhysRevB.96.235443.

9. B. A. Myers, A. Das, M. C. Dartiailh, K. Ohno, D. D. Awschalom, and A. C. B. Jayich, "Probing Surface Noise with Depth-Calibrated Spins in Diamond," *Physical Review Letter* 113, no. 2 (2014): 027602, https://doi.org/10.1103/PhysRevLett.113.027602.

10. E. Janitz, K. Herb, L. A. Völker, W. S. Huxter, C. L. Degen, and J. M. Abendroth, "Diamond Surface Engineering for Molecular Sensing with Nitrogen—Vacancy Centers," *Journal of Materials Chemistry C* 10, no. 37 (2022): 13533–13569, https://doi.org/10.1039/D2TC01258H.

11. A. Rathi, K. Oshimi, K. Sasaki, et al., "Engineering Nanodiamonds for Quantum Sensing: Material Constraints at the Nanoscale," *ACS Nano* 20, no. 24 (2026): 17143–17162, https://doi.org/10.1021/acsnano.6c03795.

12. E. Mayerhoefer and A. Krueger, "Surface Control of Nanodiamond: From Homogeneous Termination to Complex Functional Architectures for Biomedical Applications," *Accounts of Chemical Research* 55, no. 24 (2022): 3594–3604, https://doi.org/10.1021/acs.accounts.2c00596.

13. M. V. Hauf, B. Grotz, B. Naydenov, et al., "Chemical Control of the Charge State of Nitrogen-Vacancy Centers in Diamond," *Physical Review B* 83, no. 8 (2011): 081304, https://doi.org/10.1103/PhysRevB.83.081304.

14. M. Kaviani, P. Deák, B. Aradi, T. Frauenheim, J.-P. Chou, and A. Gali, "Proper Surface Termination for Luminescent Near-Surface NV Centers in Diamond," *Nano Letters* 14, no. 8 (2014): 4772–4777, https://doi.org/10.1021/nl501927y.

15. V. Petráková, A. Taylor, I. Kratochvílová, et al., "Luminescence of Nanodiamond Driven by Atomic Functionalization: Towards Novel Detection Principles," *Advanced Functional Materials* 22, no. 4 (2012): 812–819, https://doi.org/10.1002/adfm.201101936.

16. V. Petráková, M. Nesládek, A. Taylor, et al., "Luminescence Properties of Engineered Nitrogen Vacancy Centers in a Close Surface Proximity," *Physica Status Solidi(a)* 208 (2011): 2051.

17. J. Havlik, V. Petrakova, I. Rehor, et al., "Boosting Nanodiamond Fluorescence: Towards Development of Brighter Probes," *Nanoscale* 5, no. 8 (2013): 3208, https://doi.org/10.1039/c2nr32778c.

18. A. Stacey, K. M. O'Donnell, J. Chou, et al., "Nitrogen Terminated Diamond," *Advanced Materials Interfaces* 2, no. 10 (2015): 1500079, https://doi.org/10.1002/admi.201500079.

19. J. Copak, F. Steiner, E. Fialova, et al., "Linker-Free Covalent DNA Functionalization of Quantum-Grade Nanodiamonds," *Advanced Optical Materials* 13, no. 33 (2025): 02279, https://doi.org/10.1002/adom.202502279.

20. C. Osterkamp, J. Scharpf, S. Pezzagna, et al., "Increasing the Creation Yield of Shallow Single Defects in Diamond by Surface Plasma Treatment," *Applied Physics Letters* 103, no. 19 (2013): 193118, https://doi.org/10.1063/1.4829875.

21. C. Osterkamp, J. Lang, J. Scharpf, et al., "Stabilizing Shallow Color Centers in Diamond Created by Nitrogen Delta-Doping using SF6 Plasma Treatment," *Applied Physics Letters* 106, no. 11 (2015): 113109, https://doi.org/10.1063/1.4915305.

22. T. W. Shanley, A. A. Martin, I. Aharonovich, and M. Toth, "Localized Chemical Switching of the Charge State of Nitrogen-Vacancy Luminescence Centers in Diamond," *Applied Physics Letters* 105, no. 6 (2014): 063103, https://doi.org/10.1063/1.4883229.

23. S. Cui and E. L. Hu, "Increased Negatively Charged Nitrogen-Vacancy Centers in Fluorinated Diamond," *Applied Physics Letters* 103, no. 5 (2013): 051603, https://doi.org/10.1063/1.4817651.

24. J. Havlik, H. Raabova, M. Gulka, et al., "Benchtop Fluorination of Fluorescent Nanodiamonds on a Preparative Scale: Toward Unusually Hydrophilic Bright Particles," *Advanced Functional Materials* 26, no. 23 (2016): 4134–4142, https://doi.org/10.1002/adfm.201504857.

25. H. Touhara and F. Okino, "Property Control of Carbon Materials by Fluorination," *Carbon* 38, no. 2 (2000): 241–267, https://doi.org/10.1016/S0008-6223(99)00140-2.

26. E. T. Mickelson, C. B. Huffman, A. G. Rinzler, R. E. Smalley, R. H. Hauge, and J. L. Margrave, "Fluorination of Single-Wall Carbon Nanotubes," *Chemical Physics Letters* 296, no. 1-2 (1998): 188–194, https://doi.org/10.1016/S0009-2614(98)01026-4.

27. M. Adamska and U. Narkiewicz, "Fluorination of Carbon Nanotubes—A Review," *Journal of Fluorine Chemistry* 200 (2017): 179–189, https://doi.org/10.1016/j.jfluchem.2017.06.018.

28. Y.-S. Lee, *New Fluorinated Carbons: Fundamentals and Applications* (Elsevier, 2017), 135–154, https://doi.org/10.1016/B978-0-12-803479-8.00006-1.

29. T. Hasebe, S. Yohena, A. Kamijo, et al., "Fluorine Doping Into Diamond-Like Carbon Coatings Inhibits Protein Adsorption And Platelet Activation," *Journal of Biomedical Materials Research* 83A (2007): 1192–1199.

30. L. Mayrhofer, G. Moras, N. Mulakaluri, S. Rajagopalan, P. A. Stevens, and M. Moseler, "Fluorine-Terminated Diamond Surfaces as Dense Dipole Lattices: The Electrostatic Origin of Polar Hydrophobicity," *Journal of the American Chemical Society* 138, no. 12 (2016): 4018–4028, https://doi.org/10.1021/jacs.5b04073.

31. M. Cametti, B. Crousse, P. Metrangolo, R. Milani, and G. Resnati, "The Fluorous Effect in Biomolecular Applications," *Chemical Society Reviews* 41, no. 1 (2011): 31–42, https://doi.org/10.1039/C1CS15084G.

32. J. Cai, A. Retzker, F. Jelezko, and M. B. Plenio, "A Large-Scale Quantum Simulator on a Diamond Surface at Room Temperature," *Nature Physics* 9, no. 3 (2013): 168–173, https://doi.org/10.1038/nphys2519.

33. C. P. Kealey, T. M. Klapötke, D. W. McComb, M. I. Robertson, and J. M. Winfield, "Fluorination of Polycrystalline Diamond Films and Powders. An Investigation using FTIR Spectroscopy, SEM, Energy-Filtered TEM, XPS and fluorine-18 Radiotracer Methods," *Journal of Materials Chemistry* 11, no. 3 (2001): 879–886, https://doi.org/10.1039/b006800o.

34. K. J. Rietwyk, S. L. Wong, L. Cao, et al., "Work Function and Electron Affinity of the Fluorine-Terminated (100) Diamond Surface," *Applied Physics Letters* 102, no. 9 (2013): 091604, https://doi.org/10.1063/1.4793999.

35. V. S. Smentkowski and J. T. Yates, "Fluorination of Diamond Surfaces by Irradiation of Perfluorinated Alkyl Iodides," *Science* 271, no. 5246 (1996): 193–195, https://doi.org/10.1126/science.271.5246.193.

36. T. Gray, X. Zhang, A. Biswas, et al., "Benchmarking Diamond Surface Preparation and Fluorination Via Inductively Coupled Plasma-Reactive Ion Etching," *Carbon* 228 (2024): 119366, https://doi.org/10.1016/j.carbon.2024.119366.

37. C. J. Widmann, C. Giese, M. Wolfer, S. Kono, and C. E. Nebel, "F-and Cl-terminations of (100)-Oriented Single Crystalline Diamond," *Physica Status Solidi(a)* 211 (2014): 2328.

38. T. Kondo, H. Ito, K. Kusakabe, et al., "Characterization and Electrochemical Properties of CF_4 Plasma-Treated Boron-Doped Diamond Surfaces," *Diamond and Related Materials* 17, no. 1 (2008): 48–54, https://doi.org/10.1016/j.diamond.2007.10.009.

39. L. Zhao, X. Wang, M. Jiang, et al., "Optimization of Diamond Polishing Process for Sub-Nanometer Roughness Using $Ar/O_2/SF_6$ Plasma," *Materials* 18, no. 11 (2025): 2615, https://doi.org/10.3390/ma18112615.

40. S. Stehlik, M. Mermoux, B. Schummer, et al., "Size Effects on Surface Chemistry and Raman Spectra of Sub-5 nm Oxidized High-Pressure High-Temperature and Detonation Nanodiamonds," *Journal of Physical Chemistry C* 125, no. 10 (2021): 5647–5669, https://doi.org/10.1021/acs.jpcc.0c09190.

41. S. Turner, O. Shenderova, F. Da Pieve, et al., "Aberration-Corrected Microscopy and Spectroscopy Analysis of Pristine, Nitrogen Containing Detonation Nanodiamond," *Physica Status Solidi* 210 (2013): 1976.

42. V. Nesvizhevsky, U. Köster, M. Dubois, et al., "Fluorinated Nanodiamonds as Unique Neutron Reflector," *Carbon* 130 (2018): 799–805, https://doi.org/10.1016/j.carbon.2018.01.086.

43. Z. Luo, Q. Wan, Z. Yu, S. Lin, Z. Xie, and X. Wang, "Photo-Fluorination of Nanodiamonds Catalyzing Oxidative Dehydrogenation Reaction of Ethylbenzene," *Nature Communications* 12, no. 1 (2021): 6542, https://doi.org/10.1038/s41467-021-26891-8.

44. Y. Liu, Z. Gu, J. L. Margrave, and V. N. Khabashesku, "Functionalization of Nanoscale Diamond Powder: Fluoro-, Alkyl-, Amino-, and Amino Acid-Nanodiamond Derivatives," *Chemistry of Materials* 16, no. 20 (2004): 3924–3930, https://doi.org/10.1021/cm048875q.

45. M. A. Ray, O. Shenderova, W. Hook, et al., "Cold Plasma Functionalization of Nanodiamond Particles," *Diamond and Related Materials* 15, no. 11 (2006): 1809–1812, https://doi.org/10.1016/j.diamond.2006.06.003.

46. A. M. Panich, H.-M. Vieth, A. I. Shames, N. Froumin, E. Ôsawa, and A. Yao, "Structure and Bonding in Fluorinated Nanodiamond," *Journal*

of Physical Chemistry C 114, no. 2 (2010): 774–782, https://doi.org/10.1021/jp9078629.

47. K. Henry, M. Emo, S. Diliberto, et al., "Detonation Nanodiamonds with Ultrapure Surfaces through a Combined Chlorine and Fluorine Gas Treatment," *Journal of Materials Chemistry A* 14, no. 24 (2026): 15386–15406, https://doi.org/10.1039/D5TA08349D.

48. V. N. Khabashesku, V. P. Filonenko, R. K. Bagramov, A. S. Anokhin, E. V. Kukueva, and O. V. Kuznetsov, "Impact of Surface Fluorination on Phase Stability of Nanodiamond Particles and Inter-Granular Bonding in Polycrystalline Diamond Under HPHT Conditions," *Diamond and Related Materials* 112 (2021): 108247, https://doi.org/10.1016/j.diamond.2021.108247.

49. T. Ando, J. Tanaka, M. Ishii, et al., "Diffuse Reflectance Fourier-Transform Infrared Study of the Plasma-Fluorination of Diamond Surfaces Using a Microwave Discharge in CF_4," *Journal of the Chemical Society Faraday Transactions* 89, no. 16 (1993): 3105, https://doi.org/10.1039/ft9938903105.

50. T. Ando, K. Yamamoto, M. Matsuzawa, et al., "Direct Interaction of Elemental Fluorine with Diamond Surfaces," *Diamond and Related Materials* 5, no. 9 (1996): 1021–1025, https://doi.org/10.1016/0925-9635(96)00521-3.

51. E. M. Zagrebina, A. V. Generalov, A. Y. Klyushin, et al., "Comparative NEXAFS, NMR, and FTIR Study of Various-Sized Nanodiamonds: As-Prepared and Fluorinated," *Journal of Physical Chemistry C* 119, no. 1 (2015): 835–844, https://doi.org/10.1021/jp510618s.

52. T. Ando, M. Nishitani-Gamo, R. E. Rawles, K. Yamamoto, M. Kamo, and Y. Sato, "Chemical Modification of Diamond Surfaces using a Chlorinated Surface as an Intermediate State," *Diamond and Related Materials* 5, no. 10 (1996): 1136–1142, https://doi.org/10.1016/0925-9635(96)00529-8.

53. S. Sangtawesin, B. L. Dwyer, S. Srinivasan, et al., "Origins of Diamond Surface Noise Probed by Correlating Single-Spin Measurements with Surface Spectroscopy," *Physical Review X* 9 (2019): 031052.

54. M. Gulka, P. Balasubramanian, E. Shagieva, et al., "Surface Optimization of Nanodiamonds using Non-Thermal Plasma," *Carbon* 224 (2024): 119062, https://doi.org/10.1016/j.carbon.2024.119062.

55. A. Wolcott, T. Schiros, M. E. Trusheim, et al., "Surface Structure of Aerobically Oxidized Diamond Nanocrystals," *Journal of Physical Chemistry C* 118, no. 46 (2014): 26695–26702, https://doi.org/10.1021/jp506992c.

56. T. Ando, S. Inoue, M. Ishii, et al., "Fourier-Transform Infrared Photoacoustic Studies of Hydrogenated Diamond Surfaces," *Journal of the Chemical Society Faraday Transactions* 89, no. 4 (1993): 749, https://doi.org/10.1039/ft9938900749.

57. T. Ando, M. Ishii, M. Kamo, and Y. Sato, "Thermal Hydrogenation of Diamond Surfaces Studied by Diffuse Reflectance Fourier-Transform Infrared, Temperature-Programmed Desorption and Laser Raman Spectroscopy," *Journal of the Chemical Society Faraday Transactions* 89, no. 11 (1993): 1783, https://doi.org/10.1039/ft9938901783.

58. J. Mikesova, D. Miliaieva, P. Stenclova, et al., "Nanodiamonds as Traps for Fibroblast Growth Factors: Parameters Influencing the Interaction," *Carbon* 195 (2022): 372–386, https://doi.org/10.1016/j.carbon.2022.04.017.

59. P. J. Sandoval, K. Lopez, A. Arreola, et al., "Quantum Diamonds at the Beach: Chemical Insights into Silica Growth on Nanoscale Diamond using Multimodal Characterization and Simulation," *ACS Nanoscience Au* 3 (2023): 462.

60. J. F. Morar, F. J. Himpsel, G. Hollinger, G. Hughes, and J. L. Jordan, "Observation of a C-1 s Core Exciton in Diamond," *Physical Review Letter* 54 (1985): 1960.

61. A. I. Ahmed, S. Mandal, L. Gines, O. A. Williams, and C.-L. Cheng, "Low Temperature Catalytic Reactivity of Nanodiamond in Molecular Hydrogen," *Carbon* 110 (2016): 438–442, https://doi.org/10.1016/j.carbon.2016.09.019.

62. S. Y. Ong, M. Chipaux, A. Nagl, and R. Schirhagl, "Shape and Crystallographic Orientation of Nanodiamonds for Quantum Sensing," *Physical Chemistry Chemical Physics* 19, no. 17 (2017): 10748–10752, https://doi.org/10.1039/C6CP07431F.

63. S. Eldemrdash, G. Thalassinos, A. Alzahrani, et al., "Fluorescent HPHT Nanodiamonds have Disk- and Rod-Like Shapes," *Carbon* 206 (2023): 268–276, https://doi.org/10.1016/j.carbon.2023.02.018.

64. P. Reineck, L. F. Trindade, J. Havlik, et al., "Not All Fluorescent Nanodiamonds Are Created Equal: A Comparative Study," *Particle & Particle Systems Characterization* 36, no. 3 (2019): 1900009, https://doi.org/10.1002/ppsc.201900009.

65. H. Wen, D. Kordahl, I. C. Kuschnerus, et al., "Correlative Fluorescence and Transmission Electron Microscopy Assisted by 3D Machine Learning Reveals Thin Nanodiamonds Fluoresce Brighter," *ACS Nano* 17, no. 17 (2023): 16491–16500, https://doi.org/10.1021/acsnano.3c00857.

66. C. Yu, K. Shi, J. Ning, and J. Liu, "Preparation of Modified Fluorographene Oxide With Interlayer Supporting Structure," *Polymers* 13, no. 18 (2021): 3126, https://doi.org/10.3390/polym13183126.

67. K. Xu, K. Elkaduwe, R. Khan, et al., "Nanoscale Color Center Sensing of Adsorbed Water in Contact with Oil," *Advanced Functional Materials* 36, no. 13 (2026): 17457, https://doi.org/10.1002/adfm.202517457.

68. D. Bluvstein, Z. Zhang, and A. C. B. Jayich, "Identifying and Mitigating Charge Instabilities in Shallow Diamond Nitrogen-Vacancy Centers," *Physical Review Letters* 122, no. 7 (2019): 076101, https://doi.org/10.1103/PhysRevLett.122.076101.

69. I. C. Barbosa, J. Gutsche, and A. Widera, "Impact of Charge Conversion on NV-center Relaxometry," *Physical Review B* 108, no. 7 (2023): 075411, https://doi.org/10.1103/PhysRevB.108.075411.

70. Y. Mindarava, R. Blinder, C. Laube, et al., "Efficient Conversion of Nitrogen to Nitrogen-Vacancy Centers in Diamond Particles with High-Temperature Electron Irradiation," *Carbon* 170 (2020): 182–190, https://doi.org/10.1016/j.carbon.2020.07.077.

71. T. F. Segawa and A. I. Shames, "How to Identify, Attribute, and Quantify Triplet Defects in Ensembles of Small Nanoparticles," *Journal of Physical Chemistry Letters* 11, no. 17 (2020): 7438–7442, https://doi.org/10.1021/acs.jpclett.0c01922.

72. G. Thalassinos, D. J. McCloskey, A. Mameli, et al., "Robust Quantification of the Diamond Nitrogen-Vacancy Center Charge State via Photoluminescence Spectroscopy," *APL Photonics* 10, no. 10 (2025): 101102, https://doi.org/10.1063/5.0284237.

73. Y. Bao, M. Gulka, P. Kumar, et al., "Quantum-Grade Nanodiamonds from a Single-Step, Industrial-Scale Pressure and Temperature Process," *Advanced Functional Materials* 36 (2025): 20907.

74. J. Prooth, M. Petrov, A. Shmakova, et al., "Long Spin Relaxation Times in CVD-Grown Nanodiamonds," *Advanced Quantum Technologies* 6, no. 12 (2023): 2300004, https://doi.org/10.1002/qute.202300004.

75. E. K. Brown, Z. R. Jones, A. Sarkar, B. J. Wallace, A. Ajoy, and K. R. Wilson, "Quantum Sensing of Paramagnetic Analytes by Nanodiamonds in Levitated Microdroplets and Aqueous Solutions," *Chemical Science* 16, no. 41 (2025): 19328–19341, https://doi.org/10.1039/D5SC04108B.

76. S. Iyer, C. Yao, O. Lazorik, et al., "Optically-Trapped-Nanodiamond Relaxometric Detection of Nanomolar Paramagnetic Spins in Aqueous Environments," *Physical Review Applied* 22, no. 6 (2024): 064076, https://doi.org/10.1103/PhysRevApplied.22.064076.

77. J.-P. Tetienne, T. Hingant, L. Rondin, et al., "Spin Relaxometry of Single Nitrogen-Vacancy Defects in Diamond Nanocrystals for Magnetic Noise Sensing," *Physical Review B* 87, no. 23 (2013): 235436, https://doi.org/10.1103/PhysRevB.87.235436.

Supporting Information

Additional supporting information can be found online in the Supporting Information section.

Supporting File: advs78782-sup-0001-SuppMat.docx.